

Electromagnetic Analysis and Steady-State Performance of Double-Sided Flat Linear Motor Using Soft Magnetic Composite

Young-shin Kwon, *Student Member, IEEE*, and Won-jong Kim, *Senior Member, IEEE*

Abstract—The applicability of a soft magnetic composite (SMC) material to a new double-sided buried-type interior permanent-magnet flat linear brushless motor (IPM-FLBM) with slot-phase shift is presented through the steady-state performance improvement in this paper. The IPM-FLBM using a conventional electrical solid steel is used as a base model prototype for the performance comparison. The analytic models for armature resistance, inductances of series-connected asymmetric dual three-phase windings, no-load flux linkages, and back electromotive forces (back EMFs) are investigated to derive a closed-form equation for the thrust force. The magnetic field capability due to the design parameter changes of the new SMC prototype is analyzed using two simplified nonlinear magnetic equivalent circuit (MEC) models, comparing with the base model prototype. The iron and copper losses of the SMC prototype also are investigated in terms of the thermal limitation. The steady-state performance enhanced by the reduced air-gap size is experimentally validated through the comparison of the static thrust force with that of the base model prototype.

Index Terms—Alternate teeth windings, asymmetric dual three-phase motor, interior permanent-magnet flat linear motor, soft magnetic composite (SMC).

I. INTRODUCTION

IN THE past decade, many linear motion-control platforms based on conventional rotary actuators have been replaced with linear motors with high-force density, fast dynamics, and simple structure. Recently, they have become indispensable components that produce the mechanical power in various applications such as factory automation equipment, scientific apparatuses, and electric trains. Such linear motors can be classified into the air-core and iron-core types. Most iron-core types use the laminated thin silicon steel sheets as the soft magnetic material for the minimization of the eddy-current loss. In order to overcome such drawbacks, new powder iron-composite material was developed in the early 2000s [1]. Although this SMC material has several advantages such as low

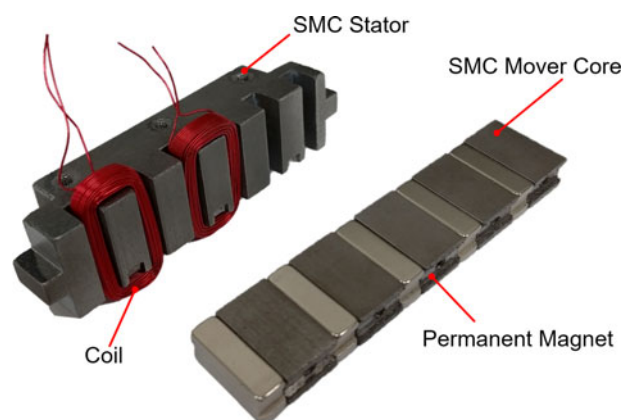


Fig. 1. Stator core with the phase coils (left) and mover with PMs (right).

eddy-current loss, flexible machine design and assembly, and three-dimensional isotropic ferromagnetic behavior, relatively good recyclability, and reduced production costs [2], its lower magnetic permeability hindered the extensive use of the SMC material in electric machines.

Thus, many studies compensating for the defect and utilizing the advantage of the SMC material have been done in the various electric machine designs over the past decade. The air-gap flux density analysis according to existence of the SMC slot closure in a PM synchronous motor (PMSM) was studied [3]. The SMC hybrid brushless direct current (BLDC) motor and SMC claw-pole motors were analyzed [4], [5]. The axial-flux PMSM was introduced [6], [7]. The design optimization for a tubular linear motor using the SMC was investigated with a finite-element analysis (FEA) [8]. An axial-flux PM machine using SMC wedge was introduced in [9].

In this sense, the steady-state performance improvement in a buried-type interior permanent-magnet flat linear brushless motor (IPM-FLBM) using a Somaloy prototyping material (SPM) is studied in this paper. The closed-form force equation of the double-sided IPM-FLBM with slot-phase shift is derived. The magnetic-field capability due to the key design parameters of the IPM-FLBM is investigated using two simplified nonlinear MECs under various electrical load conditions, comparing with the base model prototype using an electrical solid steel. The improved steady-state performance of the SPM prototype is verified through the comparison of the thrust forces in the analytic solution and measurements. Fig. 1 shows the stator and mover cores of the IPM-FLBM prototype machined using the SPM.

Manuscript received March 20, 2016; revised July 2, 2016 and August 16, 2016; accepted September 11, 2016. Date of publication October 20, 2016; date of current version February 9, 2017.

The authors are with the Department of Mechanical Engineering, Texas A&M University, College Station, TX 77843 USA (e-mail: y.s.kwon@tamu.edu; wjkim@tamu.edu).

Color versions of one or more of the figures in this paper are available online at <http://ieeexplore.ieee.org>.

Digital Object Identifier 10.1109/TIE.2016.2619658

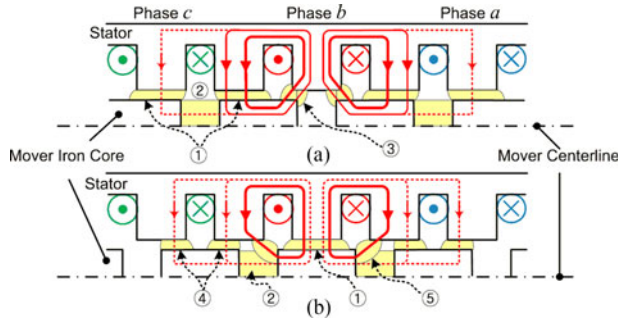


Fig. 3. Air-gap permeance models when the phase b is an armature MMF source: (a) the q -axis is aligned with the tooth center of phase b and (b) the d -axis is aligned with the tooth center of phase b .

Assuming that the permeance of the iron core is infinite under the unsaturation condition, the magnetizing inductances of the self- and mutual inductances can be obtained from the q - and d -axis air-gap permeances in the single-sided IPM-FLBM model shown in Fig. 3.

The q - and d -axis magnetizing inductances of phase b can be given, respectively, as

$$L_{qm} = L_{os} + L_{2s} \cong \frac{2N^2 (P_1 + P_2)}{P_1 P_2 \left((P_1 || P_1 || P_2)^{-1} (P_1 || P_3)^{-1} - P_1^{-2} \right)} \quad (6)$$

$$L_{dm} = L_{os} - L_{2s} \cong \frac{2N^2}{(P_1 || P_2 || P_5) \left((P_1 || P_2 || P_5)^{-1} (P_1 || P_1 || P_5)^{-1} - P_5^{-2} \right)} \quad (7)$$

where permeances P_1 , P_2 , P_3 , P_4 , and P_5 are given as

$$P_1 = 2 P_4 \cong \frac{\mu_0 D_s (T_t + T_p - T_m)}{2\delta} \quad (8)$$

$$P_2 \cong \frac{\mu_0 \mu_m D_s H_m}{0.95 T_m} \quad (9)$$

$$P_3 \cong 2\mu_0 D_s \left[\frac{T_t - T_m}{4\delta} + \frac{2}{\pi} \left(1 + \ln \left(\frac{\pi H_t}{18\delta} \right) \right) \right] \quad (10)$$

$$P_5 \cong \frac{\mu_0 D_s (0.125 T_t + 0.25 H_m)}{\pi (T_m + 0.5 H_m + \delta)}. \quad (11)$$

From (3) to (11), the parameters L_{ls} , L_{os} , and L_{2s} can be evaluated. As a result, the self-inductance function of phase b in the double-sided model with the slot-phase shift can be written as

$$L_{bb}(x_m) = 2L_{ls} + 2L_{os} + 2L_{2s} \cos(2\pi\alpha_s/T_p) \cos(2\pi x_m/T_p) \quad (12)$$

where the first cosine term is the coefficient due to the slot-phase shift. The magnetizing inductance functions for other phases are shifted by $\pm 120^\circ$ electrically from phase b . The mutual

inductances L_{ba} and L_{bc} in Fig. 3 can be expressed as

$$L_{ba..q} = L_{bc..q} \cong \frac{N^2}{P_1 \left((P_1 || P_1 || P_2)^{-1} (P_1 || P_3)^{-1} - P_1^{-2} \right)} \quad (13)$$

$$L_{ba..d} = L_{bc..d} \cong \frac{N^2}{2P_5 \left((P_1 || P_2 || P_5)^{-1} (P_1 || P_1 || P_5)^{-1} - P_5^{-2} \right)}. \quad (14)$$

Since the mutual inductances in two different positions have the interval of π , a half of the sum of two inductances is the average mutual inductance, and the reduced magnitude ratio of the mutual inductance that is $2T_s$ away from the armature MMF source can be calculated by

$$m = (L_{bc..q} + L_{bc..d}) / (L_{mq} + L_{md}). \quad (15)$$

Consequently, the mutual inductance L_{bc} is given as

$$L_{bc}(x_m) = -2mL_{os} + 2mL_{2s} \cos(2\pi\alpha_s/T_p) \times \cos\left(\frac{2\pi}{T_p}x_m - 120^\circ\right). \quad (16)$$

The two other mutual inductances are shifted by electrically $\pm 120^\circ$ from L_{bc} . However, since the L_{ac} has the distance of $4T_s$ due to the open-circuit structure of linear motor's stator, its magnitude can be approximated as

$$L_{ca}(x_m) = -2m^2L_{os} + 2m^2L_{2s} \cos(2\pi\alpha_s/T_p) \cos\left(\frac{2\pi}{T_p}x_m\right). \quad (17)$$

C. No-Load Flux Linkage and Back-EMF Voltage

In PM machines, since the no-load flux linkage is the main source to generate the thrust force, its evaluation is very important. Generally, its magnitude can be maximized when the d -axis of the mover is aligned with the centerline of the winding tooth [14], [15]. However, as shown in Fig. 2, since the same phase windings connected in series in the upper and lower stators are placed in the teeth's centerlines shifted by $+\alpha_s$ and $-\alpha_s$, respectively, the resultant maximum no-load flux linkages in each phase are developed in the new centerline of overlapped section of the upper and lower stator teeth. The resultant no-load flux linkage of the phase b can be represented using a Fourier series

$$\lambda_{pm.b}(x_m) = \frac{4B_\delta D_s N P_{avg} T_p}{\pi} \sum_n \frac{N_n B_n}{n} \sin\left(\frac{n\pi}{T_p}x_m\right) \quad (18)$$

where N is the number of turns per winding and B_n the Fourier coefficient of the air-gap flux density distribution function is described as

$$B_n = \frac{8\sin(n\pi/2)\cos\left(\frac{n\pi(T_p - T_m)}{2T_p}\right)}{n\pi} \left/ \left(\frac{n\pi(T_p - T_m)}{2T_p} \right) \right., \quad (19)$$

the winding factor N_n for the superimposed rectangular winding function is given as

$$N_n = \sin\left(\frac{n\pi T_s}{2T_p}\right) \cos\left(\frac{n\pi\alpha_s}{2T_p}\right) \sin\left(\frac{n\pi T_{so}}{2T_p}\right) \left/ \left(\frac{n\pi T_{so}}{2T_p} \right) \right. \quad (20)$$

and P_{avg} is the unitless average value of the relative permeance function of the slotted stator, which is given as

$$P_{\text{avg}} = \frac{1}{T_p} \int_{-T_s/2}^{T_s/2} P(x_s) dx_s = 0.8037 \quad (21)$$

where T_{so} is $T_s - T_t$. The relative permeance function $P(x_s)$ is described in the Appendix. The phase-to-neutral back EMF of phase b can be derived by differentiating the no-load flux linkage in (18) for the mover displacement x_m with respect to time as follows:

$$e_{\text{phase}}(x_m) = 4B_\delta D_s N P_{\text{avg}} V_m \sum_{n=1} N_n B_n \cos(n\pi x_m / T_p) \quad (22)$$

where V_m (m/s) is the mover speed. The voltages induced in other phases are shifted by $\pm 120^\circ$ electrically from phase b .

D. Steady-State Thrust Force

If the torque equation of the rotary PM BLAC motor of [11] is employed, the steady-state thrust force developed in the double-sided IPM-FLBM can be expressed in terms of the d - and q -axis current variables as follows:

$$F_x = (3\pi/2T_p) (\lambda_m I_{qs} + (L_d - L_q)I_{ds}I_{qs}) \quad (23)$$

where λ_m is $\lambda_{pm,b}$ in (18), I_q and I_d are the q - and d -axis currents. The q -axis inductance L_q and d -axis inductance L_d are given as $4L_u + 2L_{ew} + 2L_{os} + 2L_{2s} \cos(2\pi\alpha_s/T_p)$ and $2L_u + 2L_{ew} + 2L_{os} - 2L_{2s} \cos(2\pi\alpha_s/T_p)$, respectively, from the maximum and minimum values of (12). The first and second terms of the right-hand side of (23) are the magnetizing and reluctance forces, respectively.

III. ELECTROMAGNETIC ANALYSIS

Although the base model prototype using the electrical solid steel was designed in order to minimize its detent force at a nonsaturation level under the 20-A electrical load condition, if the same design dimensions are employed in the SPM prototype without the design parameter modification, the stator tooth and mover core fluxes as well as the air-gap flux density have smaller values than those of the base model prototype under both no-load and electrical load conditions because of the SMC material's low permeability. In this section, hence, the magnetic-field variations according to the design parameter modification is studied using two simplified MECs in order to improve the steady-state performance of the SPM prototype.

A. Simplified Nonlinear Magnetic Equivalent Circuit

Unlike the conventional rotary motor, the linear motor has the longitudinal end-effect leakage flux due to the open circuit of the end frame of the finite-length stator. This causes the undesired end-effect force varying with the period of the pole pitch. However, since this end-effect leakage is minimized in a locally well-balanced specific position, an infinitely long stator model without the end-effect leakage can be employed in this specific position. In this paper, therefore, a single-sided model is chosen when the d -axis is aligned with the tooth centerline of phase b with respect to the horizontal centerline of the mover shown

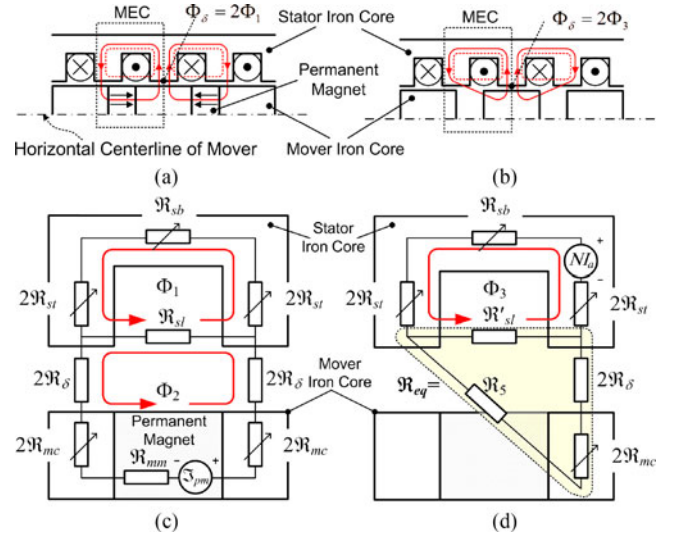


Fig. 4. Flux paths of the single-sided models due to (a) PM and (b) armature current when the d -axis is aligned with the stator tooth centerline of phase b . Corresponding simplified nonlinear MEC models under (c) the no-load condition and (d) the electrical load condition.

in Fig. 2. In addition, since the magnetic fluxes are symmetric with respect to the vertical centerline of the tooth, the half flux-path models in the dashed boxes of Fig. 4(a) and (b) can be used according to the no-load and electrical load conditions, respectively. Since the flux path due to the armature current is partially different from that of the PM, it is not easy to apply a single circuit model. Therefore, the flux values under the no-load condition in Fig. 4(c) are calculated according to the design parameters, and then the stator tooth flux Φ_1 is used as the initial value to compute the ingoing flux Φ_3 into the stator tooth under the electrical load condition of Fig. 4(d). The factor 2 is presented since the reluctance is doubled from the half-sided model. All reluctances in the stator and mover cores are defined as the variable reluctances according to the B - H curves of the corresponding core materials. From the simplified MEC model of Fig. 4(c), the fluxes in the stator and mover cores under the no-load condition can be written as a reluctance matrix and the magnetomotive forces (MMFs) generated due to the PM as follows:

$$\Phi = \begin{bmatrix} \Phi_1 \\ \Phi_2 \end{bmatrix} = \mathbf{A}_R^{-1} \begin{bmatrix} 0 \\ \mathfrak{S}_{pm} \end{bmatrix} \quad (24)$$

where the reluctance matrix \mathbf{A}_R is given as

$$\mathbf{A}_R = \begin{bmatrix} \mathfrak{R}_{sb} + 4\mathfrak{R}_{st} + \mathfrak{R}_{sl} & -\mathfrak{R}_{sl} \\ -\mathfrak{R}_{sl} & 4\mathfrak{R}_\delta + 4\mathfrak{R}_{mc} + \mathfrak{R}_{mm} + \mathfrak{R}_{sl} \end{bmatrix} \quad (25)$$

and \mathfrak{S}_{pm} is the MMF of the PM, which is given as

$$\mathfrak{S}_{pm} = \frac{B_r T_m}{\mu_0 \mu_m} \quad (26)$$

where B_r is the residual flux density, μ_0 is the permeability of free space, and $\mu_m (= 1.05)$ is the relative permeability of the PM on the recoil line on its B - H curve. From the simplified MEC model of Fig. 4(d), the incoming flux into the stator tooth

is given as

$$\Phi_3 = \frac{NI_a}{\mathcal{R}_{eq} + 4\mathcal{R}_{st} + \mathcal{R}_{sb}} + \Phi_1 \quad (27)$$

where N is the number turns of a winding, I_a is the magnitude of the armature current, and \mathcal{R}_{eq} is written by

$$\mathcal{R}_{eq} = \frac{\mathcal{R}'_{sl} (2\mathcal{R}_\delta + 2\mathcal{R}_{mc} + \mathcal{R}_5)}{\mathcal{R}'_{sl} + 2\mathcal{R}_\delta + 2\mathcal{R}_{mc} + \mathcal{R}_5} \quad (28)$$

where \mathcal{R}_5 is the inverse of P_5 . The air-gap reluctance with the symmetric fringing flux path with respect to the tooth centerline when the d -axis is aligned with the stator tooth centerline can be expressed as [16]

$$\mathcal{R}_\delta \cong \mu_0 D_m \left[\frac{T_t}{\delta} + \frac{4}{\pi} \left(1 + \ln \left(\frac{\pi H_t}{4\delta} \right) \right) \right]^{-1}. \quad (29)$$

The reluctance of the PM is calculated as

$$\mathcal{R}_{mm} = \frac{T_m}{0.775 \mu_0 \mu_m H_m D_m}. \quad (30)$$

The factor 0.775 was introduced to describe the effective contact face area reduced due to the PM with the H-shaped cross-section and all round edges with the radius of about 0.5 mm. The slot leakage reluctances are given by

$$\mathcal{R}_{sl} = \frac{T_{so}}{2\mu_0 H_t D_s} \quad \text{and} \quad \mathcal{R}'_{sl} = \frac{N^2}{L_u} \quad (31)$$

where the open-slot width T_{so} is $T_s - T_t$. The mover iron core [17], stator tooth, and stator back-iron reluctances are written as

$$\mathcal{R}_{mc} = \frac{\pi}{16\mu_0 \mu_{cm} D_m} \quad (32)$$

$$\mathcal{R}_{st} = \frac{H_s + H_t}{2\mu_0 \mu_{cs} T_t D_s} \quad (33)$$

$$\mathcal{R}_{sb} = \frac{T_s}{\mu_0 \mu_{cs} (H_s - H_t) D_s} \quad (34)$$

where μ_{cm} and μ_{cs} are the variable relative permeabilities of the mover and stator cores, respectively. The flux densities in the stator tooth under no-load and electrical conditions can be calculated by, respectively

$$B_{s1} = \frac{2\Phi_1}{T_t D_s} \quad \text{and} \quad B_{s3} = \frac{2\Phi_3}{T_t D_s}. \quad (35)$$

The relative permeance values of the stator and mover cores are updated using (35) by the B - H curves of the corresponding materials. Finally, the air-gap flux density of the incoming stator tooth flux can be calculated as

$$B_\delta = 2\mu_0 \mathcal{R}_\delta \Phi_3 / \delta. \quad (36)$$

B. Magnetic-Field Analysis

Since the magnetizing thrust force of (23) is determined by the no-load flux linkage and armature current, the magnetic-field analysis for the ingoing flux into the stator tooth is very important. Fig. 5 shows that the SPM prototype has lower flux values than those of the base model prototype when the SPM prototype has the same design parameters as the base model

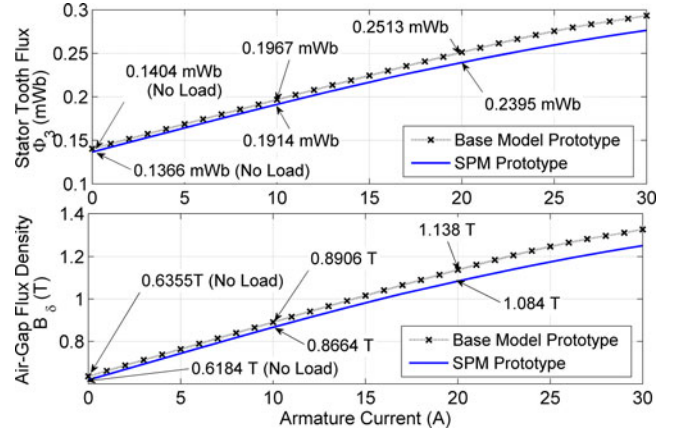


Fig. 5. Stator-tooth flux curves (top) and air-gap flux density curves (bottom) according to the armature current.

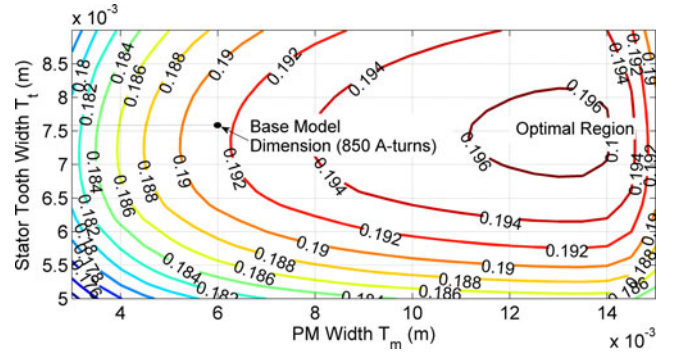


Fig. 6. Stator-tooth flux Φ_3 (mWb) contours according to the PM and stator tooth widths when $I_a = 10$ A. The total current amount can be computed as $(2) \times I_a$.

prototype. Moreover, this flux difference increases as the armature current increases. This prediction indicates that the design parameter modification is needed to produce the same or more thrust force than the base model prototype. Thus, the following constraints are made for the magnetic-field analysis of the SPM prototype: 1) the step-shaped end frame does not change; 2) the same slot pitch ($= 0.012$ m) and pole pitch ($= 0.018$ m) as those of the base model are employed to obtain the similar detent force; and 3) the open-slot width of larger than the minimum of 0.003 m is used.

1) Analysis for the PM and Stator Tooth Widths:

The possible mechanical dimensions for the stator tooth and PM widths according to the given design constraints and machinability of the PM and SPM can be given by

$$0.005 \leq T_t \leq 0.009 \quad \text{and} \quad 0.003 \leq T_m \leq 0.015 \quad (\text{m}). \quad (37)$$

The flux contours of Fig. 6 illustrate that extension of the PM width of less than 0.0013 m increases the stator tooth's flux when tooth width is around 0.0074 m. With respect to the same PM width, the tooth width of larger than 0.0074 m rather decreases the tooth flux by the reduction of the applied total current amount. Thus, if the appropriate stator tooth and PM widths are chosen depending on the required power consumption in the optimal region, the SPM prototype can obtain a larger flux than the

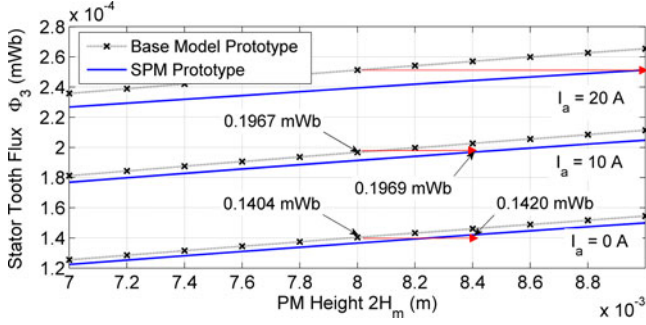


Fig. 7. Stator-tooth flux curves according to the PM height for the three different load conditions when $T_m = 0.006$ m and $T_t = 0.0076$ m.

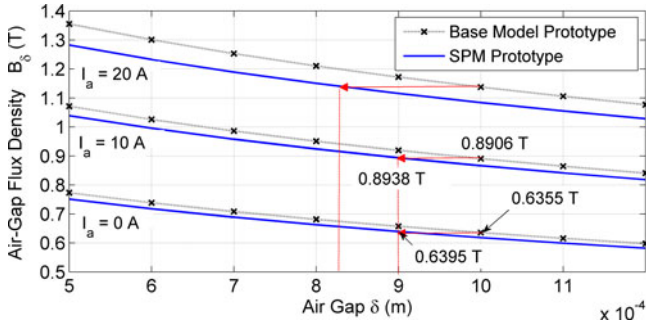


Fig. 8. Air-gap flux density curves according to the air-gap size for the three different load conditions when $T_m = 0.006$ m and $T_t = 0.0076$ m.

base model prototype under the 10-A electrical load condition. This also indicates that the base model is not fully optimized with respect to the magnetic field. The same or higher flux than the base model can be achieved through other design parameter modification.

2) Analysis for the Height of the PM and Mover Core: The MEC analysis according to the PM height in Fig. 7 shows that when the stator tooth and PM widths have the same dimensions as the base model prototype, the stator tooth fluxes in two different loads except the 20-A electrical load exhibit larger values than those of the base model prototype if the PM has the height of 0.0084 m. However, unlike the previous method presented in Section III-B.1, this approach results in the 5.0% mover weight increment due to the increased mover volume.

3) Analysis for the Air-Gap Size: The air-gap size analysis in Fig. 8 illustrates that the SPM prototype with the air-gap size of 0.0009 m can have a larger air-gap flux density than the base model prototype with the air gap of 0.001 m under the 10-A electrical load condition. Its air-gap size should also be less than 0.00083 m under the 20-A electrical load condition in order to have the same air-gap flux density as the base model prototype. This implies that the air-gap size adjustment can be a simple method to increase the air-gap flux density without the mover's weight increase or the fabrication of the newly sized PM.

4) Analysis for the Back-Iron Height: The back-iron height H_b (i.e. $H_s - H_t$) analysis in Fig. 9 shows that the air-gap flux density of the SPM prototype is hardly increased in the height of larger than 0.004 m and cannot be larger than that

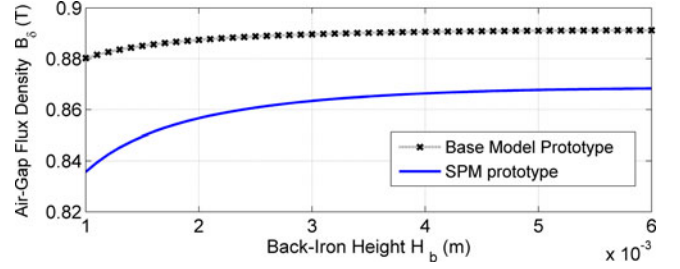


Fig. 9. Air-gap flux density variations according to the back-iron height under the 10-A electrical load condition when $T_m = 0.006$ m and $T_t = 0.0076$ m.

TABLE II
IRON LOSS PER MASS (W/kg) OF THE SPM

Flux Density (T)	Operating Frequency (Hz)									
	50	60	100	200	300	400	500	600	700	800
0.5	1.5	1.8	3.1	6.6	10	14	18	23	27	32
1.0	4.9	5.9	10	21	34	47	61	75	91	105
1.5	9.3	11	19	44	71	102	132	166	202	241

*The mass density of the SPM is 7300 kg/m³.

of the base model prototype. Therefore, this approach is not an effective way to increase the magnetic-field capability.

From the magnetic-field analysis using the simplified two nonlinear MECs, it is found that the relatively low magnetic field performance of the SPM can be improved through modifying various design parameters in the buried-type PM linear motor with a large effective air gap. In this paper, although the analysis results indicate that the method of Section III-B.1 can be improved slightly more than the method of Section III-B.3 with respect to the magnetic-field performance, the method of Section III-B.3 that can reuse the PMs of the base model is chosen in terms of cost saving and the same detent force suppression performance.

IV. LOSS ANALYSIS AND THERMAL CONSIDERATION

The iron loss is generally expressed as a form of the sum of the hysteretic loss P_h and eddy-current loss P_e . The hysteretic loss originates from the residual energy during the energy exchange by the applied current. The eddy-current loss is generated by the magnetic flux density changing in the core due to the PM. Since the SMC material does not use the lamination unlike the conventional electrical steel, the total iron loss is given as power dissipation per mass as

$$P_{\text{IRON}} = P_h + P_e = K_h B_s^a f + K_e B_s^2 f^2 \quad (\text{W/kg}) \quad (38)$$

where a varies in the range from 1.5 to 2.5, B_s is the flux density of the stator, f is the operating frequency, and K_h and K_e can be empirically determined. From Table II, K_h , K_e , and a can be evaluated as 0.092, 0.000058, and 1.6, respectively.

On the other hand, the copper loss is governed by the winding resistance and the magnitude of the phase current regardless of its operating frequency. From (1), the copper loss in the balanced

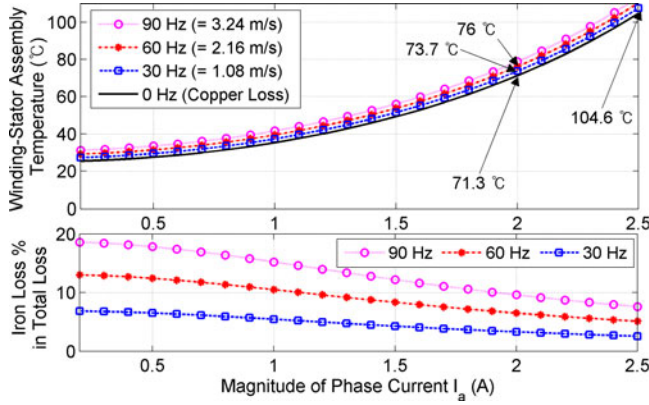


Fig. 10. Steady-state temperature responses (top) and iron-loss ratios (bottom) of the stator-winding assembly according to the phase current and operating frequency under the natural convection condition when $A_{es} = 0.0079 \text{ m}^2$ and $m_s = 0.0936 \text{ kg}$.

three-phase operation can be written as

$$P_{cu} = (3/2) I_a^2 R_c (1 + \alpha_{25} (T - 25)) \quad (\text{W}). \quad (39)$$

Assuming that the thermal contact resistance between the stator tooth and the coil is negligible, they have the same temperatures in steady state. The dissipation capability of the winding-stator assembly can be expressed with the sum of the iron and copper losses as

$$hA_{es}\Delta T = m_s P_{\text{iron}} + P_{cu} \quad (40)$$

where h is the average natural convection coefficient, m_s is the SPM stator mass, A_{es} is the effective dissipation surface area of the winding-stator assembly exposed to the air, and ΔT is the temperature rise of the winding-stator assembly. Therefore, the steady-state temperature according to the phase current can approximately be formulated using (35) and (38)–(40) as

$$T_{ss} = \frac{m_s \left(K_h (B_{s3}(I_a))^{1.6} f + K_e (B_{s3}(I_a))^2 f^2 \right) + (3/2) I_a^2 R_c}{hA_{es} - \alpha_{25} (3/2) I_a^2 R_c} + 25 \quad (41)$$

where $B_{s3}(I_a)$ is the flux-density function of (35) and h is empirically obtained from the temperature measurement in the stator winding assembly as

$$h \cong 16.1 \text{ (W/m}^2 \cdot \text{K)}. \quad (42)$$

The steady-state temperature prediction in Fig. 10 indicates that when the maximum permissible temperature is $100 \text{ }^\circ\text{C}$, the maximum continuous-rated current can be 2.4 A at 30 Hz . Although these predicted results do not include the convection coefficient variation Δh according to the mover motion, the ratio of the iron loss to the total loss in (40) does not change because this varying coefficient is evenly applied in the total loss. The iron-loss ratio in the bottom plot of Fig. 10 shows that the iron loss is not critical in the perspective of the permissible temperature limit. Although the hysteretic loss of the SMC material is relatively larger than that of the laminated thin steel,

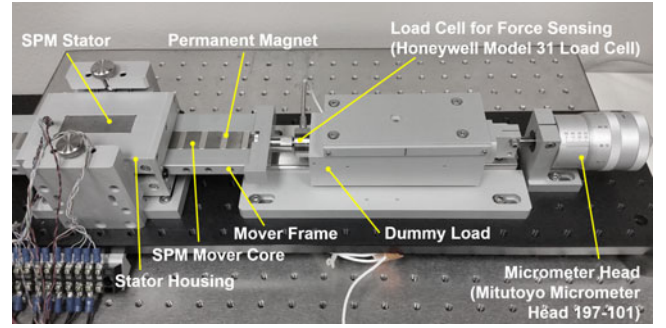


Fig. 11. Experimental setup to measure the steady-state thrust forces and inductances.

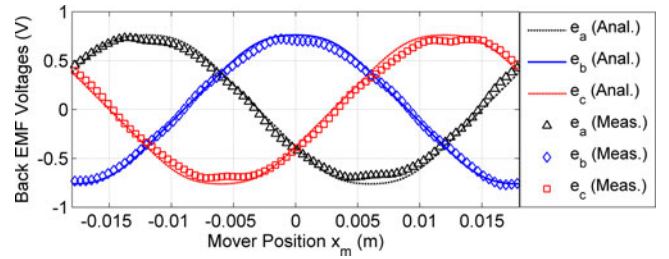


Fig. 12. Analytic and measurement results of the back EMFs for each phase when the mover has the linear speed of 0.2 m/s .

the iron loss is not the major concern in a small-size lightweight IPM-FLBM operating at a low frequency of less than 30 Hz as compared with the copper loss.

V. STEADY-STATE PERFORMANCE VALIDATION

The photograph of Fig. 11 shows the experimental setup that measures the inductances and steady-state thrust forces of the double-sided $6/4$ IPM-FLBM using the SPM material. A 300-W dc power supply was used. A precision bidirectional load cell with the 0.1% nonlinearity and a micrometer head with the accuracy of $\pm 0.0005 \text{ mm}$ were employed in order to measure the steady-state thrust forces and inductances according to the mover positions.

Fig. 12 shows that although the measured phase-to-neutral back-EMF voltages are slightly more distorted than those of the analytic solutions by the third harmonic term, they are in good agreement with the predicted ones. The back-EMF constant is estimated as $3.81 \text{ V} \cdot \text{s/m}$ per phase.

The inductances were measured using the 1.0-A current source at 60 Hz . The self-inductance distributions in Fig. 13 illustrate that each inductance has its maximum value whenever the q -axis is aligned with the resultant phase axis. Since the analytic solution assumes the permeance of the core as infinite, they seem to have 3% larger values than the measured inductances in their maximum amplitudes. Especially, these measured inductances are almost the same as those of the base model using the electrical solid steel and the air gap of 0.001 m . This points out that the self-inductances do not much increase although the air gap is reduced to be 0.0009 m . The mutual inductances in Fig. 14 show that although the amplitudes of the analytic solutions for

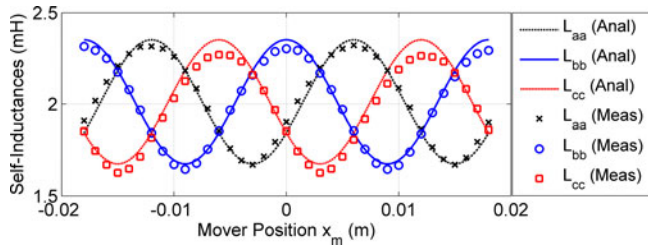


Fig. 13. Analytic and measured self-inductances of the SPM prototype with respect to positions.

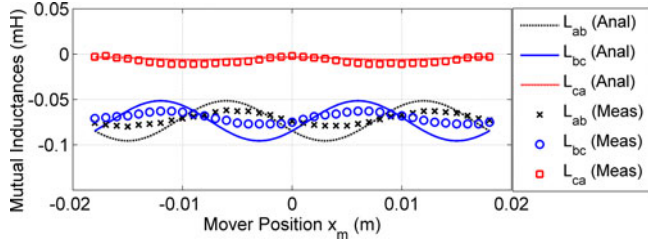


Fig. 14. Analytic and measured mutual inductances of the SPM prototype with respect to positions.

TABLE III

AVERAGE INDUCTANCES OF THE SPM AND BASE MODEL PROTOTYPES

	L_{aa}	L_{bb}	L_{cc}	L_{ab}, L_{ba}	L_{bc}, L_{cb}	L_{ac}, L_{ca}
SPM calculated (mH)	2.013	2.015	2.013	-0.074	-0.074	-0.005
SPM measured (mH)	2.022	2.006	1.973	-0.070	-0.070	-0.007
SS400 measured (mH)	2.034	2.042	1.975	-0.065	-0.067	-0.019

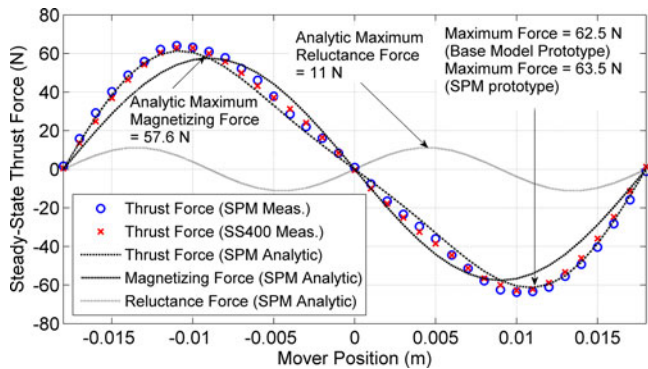


Fig. 15. Steady-state thrust forces of the SPM and base model (SS400) prototypes according to the mover positions when $I_a = 8.66$ A, $I_b = 0$ A, and $I_c = -8.66$ A.

L_{ba} and L_{cb} are twice than measured ones, their average values in Table III are very small as expected, and their trends are in good agreement with the analytic ones. This implies that the mutual inductances can be ignored in the buried-type IPM motor with the alternate teeth windings and large longitudinal air gap.

The results in Fig. 15 illustrate that the thrust force profile of the SPM prototype is slightly larger than that of the base model prototype. This implies that the magnetic flux has been increased

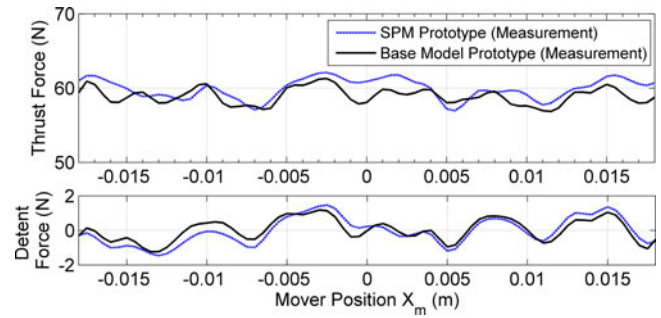


Fig. 16. Steady-state forces (top) and detent forces (bottom) of the SPM and base model (SS400) prototypes according to the mover positions when I_{qs} and I_{ds} are controlled as 10 and 0 A, respectively.

TABLE IV

PERFORMANCE COMPARISONS OF SS400 AND SPM PROTOTYPES

	Base Model	SPM
Thrust force in the field-oriented control (N)	58.9 (57.1)	59.8 (57.6)
Thrust force in the maximum force control (N)	62.5 (59.2)	63.5 (60.7)
Peak-to-peak detent force (N)	2.4	2.8
Ripple force due to the detent force (%)	4	4.7
q -Axis inductance (mH)	2.322 (2.277)	2.338 (2.352)
d -Axis inductance (mH)	1.680 (1.611)	1.671 (1.676)
Air gap (m)	0.001	0.0009

*() is the analytic solution.

by the reduced air gap. Although the developed reluctance force is not significantly large because of the small difference between the d - and q -axis inductances, the maximum thrust force can be achieved when the phase current leads the q -axis current by around 15° . The analytic magnetizing force term of (23) was computed using the maximum no-load flux linkage ($\cong 22$ mWb turns) obtained from (18), and the analytic reluctance force was calculated using the d - and q -axis inductances ($L_d = 1.676$ mH and $L_q = 2.352$ mH) obtained from the maximum and minimum values of (12). Herein, the reluctance force was predicted as around 19% of the magnetizing force. The analytic total thrust force for the SPM prototype was estimated as 3% less than both measurement results. The residual flux density of the actual PM seems to be slightly higher than the analytic model.

Unlike the conventional rotary motor, the detent force in an iron-core PM linear motor has not only the cogging force but also the end-effect force [10]. This detent force is one of the causes of the force pulsation. The top and bottom plots in Fig. 16 show the steady-state thrust forces and detent forces in the base model and SPM prototypes according to the mover positions when $I_q = 10$ A and $I_d = 0$ A and when $I_q = I_d = 0$ A, respectively. The average steady-state thrust forces of the SPM prototype are slightly improved as compared with those of the base model prototype, and the detent force is also slightly increased due to the reduced air gap in the SPM prototype. Table IV shows the steady-state performance comparisons between the two prototypes for the measurements and analytic solutions.

The measured temperature responses in Fig. 17 illustrate that when the phase current of 10 A is applied, the temperature reaches 100°C within 29 s. This implies that if the stall current is defined as 10 A when the speed of the mover is zero under

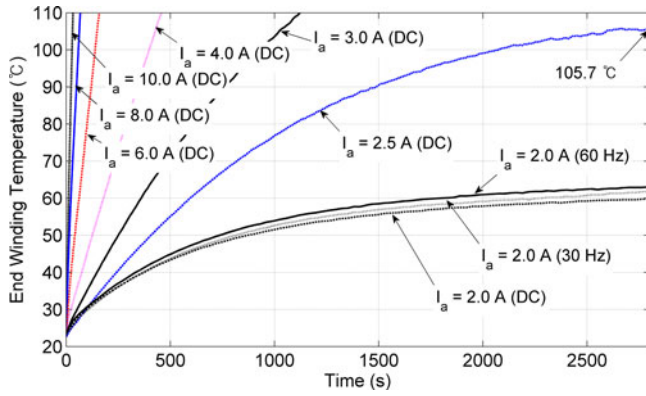


Fig. 17. Temperature responses in the end winding of the stator winding assembly according to the magnitude of the phase current and operating frequency.

TABLE V
THERMAL CONDUCTIVITY AND MATERIAL THICKNESS

Materials	Path Thickness L_n (mm)	Thermal Conductivities k_n (W/m·K)	Maximum Allowable Temperature (°C)
1 Polyurethane	0.0178	0.03	155
2 Thermal compound	0.2500	8.50	180
3 Kapton	0.0500	0.42	285

the full-load condition, the corresponding operating time should be less than 29 s in order to protect the winding insulator. The steady-state temperature for the phase currents of 2.5 A at around 2600 s is in agreement with the prediction of Fig. 10. Since the temperature according to the operating frequencies of the phase current of 2.0 A did not reach the steady-state responses, the temperature difference per 30-Hz increment was measured as around 1.5 °C. Although the difference is less than the prediction of Fig. 10, this result indicates that the iron loss is not critical in lightweight SMC motor. Table V summarizes the thermal conductivities of the materials between the winding and stator in this paper.

VI. CONCLUSION

Since the SMC material has the lower permeability, higher hysteretic loss, and lower loss at high frequency as compared with the conventional electrical steel, it has been known that the SMC material is suitable for high-frequency applications. In this paper, its applicability to the double-sided buried-type IPM motor with a large effective air gap under a low-frequency operating condition was studied in terms of the improvement of the steady-state performance. The flux linkages, back-EMFs, and series-connected inductances of the new double-sided IPM-FLBM with a slot-phase shift were analytically modeled to derive the closed-form thrust force equation. The various design parameters were studied using the two simplified nonlinear MEC models according to the load conditions without using FEA tools. The reduced air gap was chosen to improve the steady-state performance without the increase of weight and volume. Eventually, the applicability of the environment-friendly

SPM motor with the buried PMs was experimentally validated through the steady-state thrust-force comparison with the electrical steel prototypes. It was also found that the iron loss of the small-size lightweight SMC motor was not critical in terms of the temperature dissipation.

APPENDIX

The magnitude of the relative permeance function of (21) takes a value between 0 and 1, which is expressed by

$$P_s(x_s) = P_0 + (1 - P_0) \left(\frac{T_s + T_t - k_s T_{so}}{2T_s} \right) + 2(1 - P_0) \times \left(\frac{T_s}{(1 - k_s) T_{so}} \right) \sum_n P_n \cos \left(\frac{2n\pi}{T_s} x_s \right) \quad (43)$$

where the Fourier coefficients of this function are given by

$$P_n = \frac{2}{(n\pi)^2} \sin \left(\frac{n\pi (T_s + T_t - k_s T_{so})}{2T_s} \right) \times \sin \left(\frac{n\pi (1 - k_s) T_{so}}{2T_s} \right) \quad (44)$$

and P_0 and k_s are calculated as

$$P_0 = \frac{2K_{cs}u_s}{1 + u_s^2} \quad \text{and} \quad k_s \approx \frac{T_{so}}{5\delta + T_{so}} \quad (45)$$

where Carter coefficient K_{cs} and u_s are calculated as

$$K_{cs} = \frac{T_s}{T_s - T_{seo}} = \frac{T_s}{T_s - k_s T_{so}} \quad (46)$$

$$u_s = \frac{T_{so}}{2\delta} + \sqrt{1 + \left(\frac{T_{so}}{2\delta} \right)^2}$$

REFERENCES

- [1] L. O. Hultman and A. G. Jack, "Soft magnet composites-material and application," in *Proc. IEEE Int. Electron. Mach. Drives Conf.*, Jun. 2003, pp. 516–522.
- [2] H. Shokrollahi and K. Janghorban, "Soft magnetic composite materials (SMCs)," *J. Mater. Process. Technol.*, vol. 189, pp. 1–12, Jul. 2007.
- [3] G. Cvetkovski and L. Petkovska, "Performance improvement of PM synchronous motor by using soft magnetic composite material," *IEEE Trans. Magn.*, vol. 44, no. 11, pp. 3812–3815, Nov. 2008.
- [4] T. Ishikawa, K. Takahashi, Q. V. Ho, M. Matsunami, and N. Kurita, "Analysis of novel brushless DC motors made of soft magnetic composite core," *IEEE Trans. Magn.*, vol. 48, no. 2, pp. 971–974, Feb. 2012.
- [5] Y. G. Guo, J. G. Zhu, and D. G. Dorell, "Design and analysis of a claw pole permanent magnet motor with molded soft magnetic composite core," *IEEE Trans. Magn.*, vol. 45, no. 10, pp. 4582–4585, Oct. 2009.
- [6] R. D. Stefano and F. Marignetti, "Electromagnetic analysis of axial-flux permanent magnet synchronous machines with fractional windings with experimental validation," *IEEE Trans. Ind. Electron.*, vol. 59, no. 6, pp. 2573–2581, Jun. 2012.
- [7] H. Vansompel, P. Sergeant, L. Dupré, and A. den Bossche, "Axial-flux PM machines with variable air gap," *IEEE Trans. Ind. Electron.*, vol. 61, no. 2, pp. 730–737, Feb. 2014.
- [8] J. Wang, D. Howe, and Z. Lin, "Design optimization of short-stroke single-phase tubular permanent-magnet motor for refrigeration applications," *IEEE Trans. Ind. Electron.*, vol. 57, no. 10, pp. 327–334, Jan. 2010.
- [9] G. D. Donato, F. G. Capponi, and F. Caricchi, "On the use of magnetic wedges in axial flux permanent magnet machine," *IEEE Trans. Ind. Electron.*, vol. 60, no. 11, pp. 4831–4840, Nov. 2013.
- [10] Y. S. Kwon and W.-J. Kim, "Detent-force minimization of double-sided interior permanent-magnet flat linear brushless motor," *IEEE Trans. Magn.*, vol. 52, no. 4, Apr. 2016, Art. no. 8201609.

- [11] D. W. Novotny and T. A. Lipo, *Vector Control and Dynamics of AC Drives*, 1st ed. New York, NY, USA: Oxford Univ. Press, 1996.
- [12] J. Pyrhönen, T. Jokinen, and V. Hrabovcová, *Design of Rotating Electrical Machines*, 1st ed. Hoboken, NJ, USA: Wiley, 2008.
- [13] J. H. J. Potgieter and M. Kamper, "Evaluation of calculation methods and the effect of end-winding inductance on the performance of non-overlapping winding PM machines," in *Proc. 20th ICEM*, Mar. 2012, pp. 243–249.
- [14] D. Ishak, Z. Q. Zhu, and D. Howe, "Comparison of PM brushless motors, having either all teeth or alternate teeth wound," *IEEE Trans. Energy Convers.*, vol. 21, no. 1, pp. 95–100, Mar. 2006.
- [15] A. M. El-Refaie, T. M. Jahns, and D. W. Novotny, "Analysis of surface permanent magnet machines with fractional-slot concentrated windings," *IEEE Trans. Energy Convers.*, vol. 21, no. 1, pp. 34–43, Mar. 2006.
- [16] A. Balakrishnan, W. T. Joines, and T. G. Wilson, "Air-gap reluctance and inductance calculations for magnetic circuits using a Schwarz–Christoffel transformation," *IEEE Trans. Power Electron.*, vol. 12, no. 4, pp. 654–663, Jul. 1997.
- [17] J. Mühlenthaler, J. W. Kolar, and A. Ecklebe, "A novel approach for 3D air gap reluctance calculation," in *Proc. 8th IEEE ICPE, ECCE Asia*, Jun. 2011, pp. 446–452.
- [18] O. Anderson and P. Hofecker, "Advances in soft magnetic composites materials and application," in *Proc. Int. Conf. Powder Metallurgy Particulate Mater.*, Las Vegas, NV, USA, Dec. 2009, pp. 1–12.



Young-shin Kwon (S'11) received the B.S. and M.S. degrees in control and instrumentation engineering from Hanyang University and Seoul University, Seoul, South Korea, in 1995 and 1997, respectively. He is currently working towards the Ph.D. degree in the department of mechanical engineering, Texas A&M University, College Station, TX, USA.

After receiving the M.S. degree, he was a Research Engineer with Hyundai Electronics Corporation, Icheon, South Korea, for two years. He developed the RF seekers of active guided missile systems and naval/airborne radar systems as a Principal Researcher with LIG Nex1 Corporation, Yong-In, South Korea, for 13 years. His current research interests include design, analysis, and real-time control of spatial stabilization of multi-axis platforms, precision opto-mechatronics systems, and magnetic linear actuators.



Won-jong Kim (S'89–M'97–SM'03) received the B.S. (*summa cum laude*) and M.S. degrees in control and instrumentation engineering from Seoul National University, Seoul, South Korea, in 1989 and 1991, respectively, and the Ph.D. degree in electrical engineering and computer science from the Massachusetts Institute of Technology (MIT), Cambridge, MA, USA, in 1997.

Since 2000, he has been with the Department of Mechanical Engineering, Texas A&M University (TAMU), College Station, where he currently is an Associate Professor and was the inaugural Holder of the Dietz Career Development Professorship II in 2007–2010. He is the holder of three U.S. patents on precision positioning systems. He is or was a Technical Editor of the *ASME Journal of Dynamic Systems, Measurement, and Control*, the *International Journal of Control, Automation, and Systems*, and the *Asian Journal of Control*. His current research interests include the analysis, design, and real-time control of mechatronic systems, networked control systems, and nanoscale engineering and technology.

Dr. Kim is a Fellow of the American Society of Mechanical Engineers (ASME) and a Member of Pi Tau Sigma. He was Technical Editor of the IEEE/ASME TRANSACTIONS ON MECHATRONICS.